FULL PAPER

The global geomagnetic field over the historical era: what can we learn from ship-log declinations?

Maximilian Schanner[1]*![ORCID], Lukas Bohsung[2], Clara Fischer[3], Monika Korte[3] and Matthias Holschneider[4]

Abstract

Modern geomagnetic field models are constructed from satellite and observatory data, while models on the millennial timescale are constructed from indirect records of thermoremanent and sedimentary origin. An intermediate period, spanning the last four centuries, is covered by historical survey data and ship-logs, which is strongly dominated by geomagnetic declination information. We apply a sequentialized, Gaussian process-based modeling technique to this dataset and propose a new field model for this era. In order to investigate the information gained from declination records from ship-logs, we separate the dataset and construct a second model, where unpaired declination records (i.e., measurements where only declinations are reported and the rest of the field vector is missing) are removed. The availability of more records helps notably to constrain global field properties like the dipole moment. It also allows to resolve some detailed field structures more accurately. Based on the model constructed from the full dataset, we perform an analysis of the South Atlantic Anomaly and regions of low field intensity in general. We extend a recent analysis of center of mass movement and area evolution of the South Atlantic Anomaly further back in time and confirm the findings of its non-monotonous growth.

Keywords Geomagnetic field, Statistical modeling, Gaussian processes, Kalman filter, South Atlantic Anomaly, Bayesian inversion
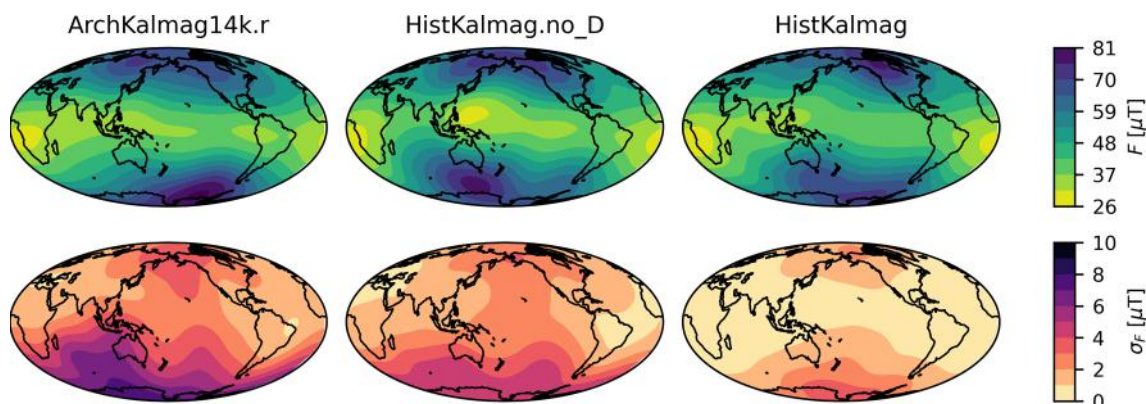
*Correspondence:
Maximilian Schanner
arthus@gfz-potsdam.de
Full list of author information is available at the end of the article

Schanner *et al. Earth, Planets and Space*   (2023) 75:96

Page 2 of 13

Graphical Abstract

Introduction

Studies of the geomagnetic field can shed light on the Earth's interior processes. By projecting global field models to the core–mantle boundary, the evolution of the geomagnetic field can be related to the core flow (Bloxham and Jackson 1992; Hulot et al. 2002; Gillet 2019). Both the geomagnetic field and the dynamo process in the liquid core exhibit a rich dynamic on multiple timescales (e.g., Constable and Korte 2015). A good worldwide data coverage is required to provide the full global view of geomagnetic field evolution. During recent times, satellite data are available and allow for the inversion of high-resolution models on the decadal timescale (e.g., Finlay et al. 2020; Alken et al. 2021; Baerenzung et al. 2022). When going back in time, data become sparse and the model resolution is limited (Hellio and Gillet 2018; Schanner et al. 2022). Still, archeomagnetic records allow for the reconstruction of the global geomagnetic field at least until 6000 BCE and together with sediment records, large-scale features of the field can be recovered on millenial and longer timescales (Constable and Korte 2015). An intermediate timescale, going back several hundred years, is covered by historical records from land surveys and ship-logs. While the former include directional and intensity measurements, the latter almost exclusively comprises declination records, that have been measured in large numbers for navigational purposes. Even though the magnetic declination contains limited information about the field vector, the ship-log dataset may provide useful information on global and regional field structure, due to its dense coverage of the oceans.

Traditionally, global geomagnetic field models are represented in the spherical harmonics expansion with a B-spline model for the time evolution. The series coefficients are determined by a regularized least squares procedure (Bloxham and Jackson 1992; Korte and Constable 2003). During recent times, statistical methods have been suggested, allowing for assessment of model uncertainties (Roman and Karl 2007; Holschneider et al. 2016; Mauerberger et al. 2020). While several bootstrapping approaches exist (Monika et al. 2011; Hellio and Gillet 2018; Patrick et al. 2019), more rigorous algorithms have been proposed recently (Schanner et al. 2021; Nilsson and Suttie 2021). Based on Gaussian process regression, the non-linear relation of directional and intensity records is either tackled via sampling or linearization. Both methods are limited by high numerical costs when considering large datasets.

In this study, we apply a sequentialized Bayesian inversion procedure (Schanner et al. 2022) to a combined dataset of archeomagnetic and historical records to construct a global field model for the past 1000 years. The main difficulty is the estimation of model parameters, as this step requires inverting the dataset multiple times. We argue, that using hyperparameters which are estimated from a longer timescale archeomagnetic dataset is reasonable and enables the application of the inversion to the larger combined dataset. By separating the ship-log declinations and performing two inversions, we illustrate what information can be inferred from declination records on a global scale.

Arneitz et al. (2021) present a model for a similar era, based on a similar database. Major differences to their work are in data selection and the inversion procedure. We compare our results to their BIGMUDIh.1 model whenever appropriate.

Methods

We construct two new global geomagnetic field models, covering the last 1000 years. The modeling procedure is similar to the construction of ArchKalmag14k and is described in detail in Schanner et al. (2022). The central idea is modeling the global geomagnetic field as a Gaussian process, i.e.,

$$\boldsymbol{B} \sim \mathcal{GP}\left(\bar{\boldsymbol{B}}, K_{\boldsymbol{B}}\right), \tag{1}$$

where $\bar{\boldsymbol{B}}$ is the mean function and $K_{\boldsymbol{B}}$ the covariance kernel. As historical and archeomagnetic records are given as directions and intensities, the field vector $\boldsymbol{B}$ is nonlinearly related to the observations. To be able to access the posterior, the observation functionals are linearized around a proxy model $\tilde{\boldsymbol{B}}$, resulting in a normal likelihood and therefore a normal approximation of the posterior distribution, thanks to a Gaussian prior. The historical dataset also contains measurements of the horizontal intensity F_H. These are handled analogously to the intensity F, i.e.:

$$F_H \approx \frac{1}{\tilde{F}_H}\left(\tilde{B}_N, \tilde{B}_E, 0\right)^{\top} \cdot \boldsymbol{B}. \tag{2}$$

Due to the amount of data, a direct Gaussian process regression is unfeasible. Instead, the inversion is sequentialized by means of a Kalman filter (Kalman 1960; Baerenzung et al. 2020). Cross-correlations are reintroduced by a smoothing step.

Dating errors are handled similar to the ArchKalmag14k-approach by using a noisy input Gaussian process (McHutchon and Rasmussen 2011). However, due to the shorter interval covered by the model, we do not expect very large field changes over the interval spanned by the dating uncertainties. (ArchKalmag14k covers 14.000 years, while the presented models only cover 1.000 years.) We therefore set upper bounds for the translated errors, in contrast to the original approach, where translated errors could become arbitrary large. The upper bounds are $30°$, $15°$, 10μT and 8μT for declination, inclination, intensity and horizontal intensity, respectively.

We start the modeling process at 1950 CE and go back until 1000 CE. New data are incorporated every year and the output stored every ten years. Similar to ArchKalmag14k, the cutoff degree (in a spherical harmonics expansion) is set to 20. This leads to an output of 440 field coefficients and 440 secular variation coefficients, together with the corresponding covariance matrix, at 96 knot points.

With the Kalman filter approach, it is straightforward to connect the model to existing ones. We choose the initial mean and covariance to agree with the Kalmag model output for 1950 CE (Kalmag spans the interval 1900 to 2022; Baerenzung et al. 2022). Besides constraining the model by incorporating knowledge from the satellite era, this has the advantage of improving the initial linearization point.

Hyperparameters

With the established algorithm, the model depends on several hyperparameters, that define the Gaussian process kernel and prior mean. These consist of two timescales, that give the temporal smoothness of the process, two variances, which control the magnitude of the field dynamics, a mean value for the axial dipole and a residual term, that is related to contributions in the measurements, which are not reflected in the model (e.g., the crustal field). To estimate these parameters, two central strategies have been pursued in the past: Hellio and Gillet (2018) and Nilsson and Suttie (2021) used reference models from the satellite era to constrain the parameters, while Schanner et al. (2022) estimated the parameters from the dataset directly. Applying the latter approach to the historical dataset is unfeasible, due to the large amount of data (about 140.000 declination records) and the resulting longer inversion times. Inversion of the full archeomagnetic dataset, used to construct the ArchKalmag14k model, takes about 30 s, but the inversion of the full combined dataset takes about two and a half hours. In order to find the optimal set of hyperparameters, around ten thousand inversions have to be performed, rendering the strategy unfeasible. Another hindrance is the timescale on which the dipole changes. Recently, Nilsson et al. (2022) found recurrent signals in the dipole moment with a period of 650 years. To reliably estimate a correlation time corresponding to these signals, multiple periods should be covered by the model. With the 1000 years covered by the dataset of this study, this is barely the case and a longer timespan will facilitate estimation of the a priori timescale. We therefore choose to set the a priori hyperparameters to the values estimated from the ArchKalmag14k.r dataset, as given in Table 1 of Schanner et al. (2022). In order to check for faster signals in the dipole, we performed an inversion with a white noise kernel (for the dipole), which amounts to neglect the time correlation in the prior for the dipole. Analysis of the posterior mean and empirical autocorrelation function indicates that the ArchKalmag14k.r prior is able to capture the variations present in the data. We further inverted the data using the two parameter kernel proposed by Bouligand et al. (2016). As this type of kernel contains two timescales with different spectral behaviors, it might be able to reflect both the millenial and the faster, centennial dynamics of the dipole. Two sets of parameters were chosen: for one model, all hyperparameters

were kept from ArchKalmag14k.r and the dipole correlation times were chosen as proposed by Hellio and Gillet (2018). The resulting model is not able to resolve the variations present in the data, most likely due to the large value of the long timescale (T_s, c.f. Hellio and Gillet (2018), above paragraph 3). For the second model, the hyperparameters were estimated from 10 percent of the full dataset (i.e., including unpaired declinations), that have been chosen randomly. The obtained parameters for the non-dipole agree well with ArchKalmag14k.r. The dipole parameters lead to a model that reproduces the posterior features of the one we get when inverting with the ArchKalmag14k.r-parameters. This contradicts our concern that 1000 years is not enough to determine the suitable dipole hyperparameters. It nevertheless supports our decision to use the a priori hyperparameters estimated from the longer archeomagnetic dataset.

Data

There are two classes of data considered in this study. Indirect measurements of the geomagnetic field are taken from the GEOMAGIA database (Brown et al. 2015, accessed 30.06.2021). The dataset consists of declination, inclination and intensity measurements from volcanic rocks and archeologic artifacts. Direct measurements stem from the HISTMAG database (Patrick et al. 2017, accessed 14.09.2022). In this database, records from land surveys, ship voyages and observatories are compiled. In addition to declination, inclination and intensity records, some historical horizontal intensity values are included. In general, the dataset is quite similar to the one used for constructing the BIGMUDIh.1 model (Arneitz et al. 2021).

A major difference to the dataset is the assessment of uncertainties. Estimating realistic, reliable uncertainties for (paleo-)magnetic measurements is a difficult task and to date no consistent strategy exists. For the indirect records, we assigned values of $\alpha_{95} = 4.5°$ to directions with missing errors and $\sigma_F = 5\mu\text{T}$ to intensities. The HISTMAG database does not contain error estimates for most of the records. For the unpaired declinations (i.e., measurements where only declinations are reported and the rest of the field vector is missing), α_{95} was converted to σ_D by assuming an axial dipole. We tested several error levels for the direct records. The error level of the intensities and inclinations has almost no influence on the model. However, we find that our modeling procedure results in unrealistically high non-dipole energies, if the error level for the declinations is chosen too low (below $\alpha_{95} = 3°$). A higher error level can be interpreted as additional regularization.

The indirect measurements are distributed equally over the time interval under consideration. Spatially, they are unevenly distributed, with clusters in Europe, East Asia and America (see Additional file 1: Figure S1). From the direct measurements, we separate records that consist of unpaired declinations. The resulting historical dataset with single declinations removed covers the last 400 years, with the majority of records in the nineteenth and twentieth century. The spatial coverage is more even than in the archeomagnetic dataset. Still, a bias towards the northern hemisphere remains. An illustration of the dataset without declinations, showing composition, spatial and temporal distribution, is given in Fig. 1. The declination dataset goes further back in time, until the sixteenth century. Except from Antarctica and some inland regions, it covers the globe densely, as declination was measured both from shipboard and on land surveys. Further illustrations of the datasets, similar to Fig. 1, are provided with the supplementary material.

Following Schanner et al. (2022), we identify outliers by means of a Naive Bayes classifier (e.g., Berrar 2018). Records that have already been identified as outliers during construction of the ArchKalmag14k.r model are removed first. Then, an inversion is performed. For every record, the probability to be generated from the model distribution or from a flat ("noise") distribution is calculated. Records that are more likely to stem from the flat distribution are discarded as outliers. This leads to the exclusion of 169 records. The small number of rejected records is likely due to the conservative error values assigned to the historical records, but also demonstrates a good internal consistency of the large historical dataset. The distribution of outliers mostly reflects the distribution of the data. The majority of rejected records are declinations, for which seemingly a minus sign has been lost during transcription. Comparison of the model with the full database and models without outliers shows only minor differences, especially on a global scale. We still reject the records. The central difference between the approach with the naive Bayes classifier and other existing approaches, is that previously data were rated before the inversion procedure (e.g., Arneitz et al. 2021), while the naive Bayes classifier is run parallel to the inversion. We give the number of records ending up in our dataset in Table 1. For comparison purposes, also the number of indirect records is given.

Results and discussion

In analogy to the Kalmag and ArchKalmag14k models, we call the presented models HistKalmag and Histkalmag.no_D, where the latter refers to the version without single declinations. Figure 2 shows the dipole and non-dipole energy of several models at the core–mantle boundary (i.e., the dipole power and the sum of all higher terms in the geomagnetic power spectrum
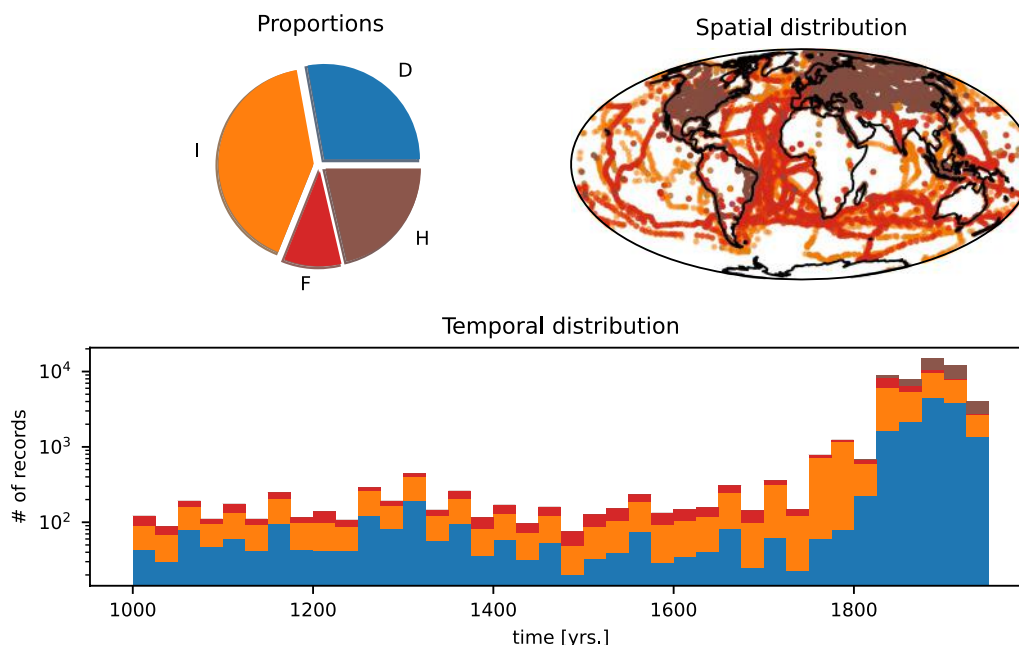
Fig. 1 Composition of the dataset with single declinations removed, together with spatial and temporal distribution

Table 1 Number of records of individual field components in several datasets

| Name	# D	# I	# F	# H	# tot
indir.	1945	3102	1477	0	6524
no_D	15,564	22,934	5413	11,935	55,846
Full	156,471	22,934	5413	11,935	196,753

"Indir." refers to indirect measurements and "no_D" to the dataset with single declinations removed. "Full" refers to the full dataset, which the HistKalmag model is built from

(e.g., Backus et al. 1996, section 4.4.2)). Both versions of HistKalmag show less variation than the comparison model BIGMUDIh.1 in the dipole, while more variation is present in the non-dipole coefficients. Before 1800 CE, when no survey data are available, the non-dipole energy of HistKalmag.no_D quickly rises to a level comparable to the ArchKalmag14k.r model. In contrast, the non-dipole contribution in the HistKalmag model rises more uniformly and reaches a similar level at around 1500 CE, when the database comprises archeological and volcanic records only. As with ArchKalmag14k.r, an explanation for this may be the global information contained in the declination records. There, the limited global information and causes the model to resolve observations locally, by higher spherical harmonic degrees. However, investigating the power spectrum (Additional file 1: Figures S3–S5) shows, that higher order degrees are also resolved by both HistKalmag models. The information contained in the declination dataset may result in a more realistic

recovery of the higher order degrees and therefore a more moderate decline towards the present value. An argument for this effect instead of the better resolution of global degrees is the good agreement of the dipole energies between all three -Kalmag models. The deviance between ArchKalmag14k.r and the HistKalmag models prior to 1400 CE, where the database is the same, is due to the slight modification of the noisy input Gaussian process (i.e., the constraint translated dating errors) mentioned above.

Figure 3 shows the global field intensity and standard deviation for the epoch 1700 CE. The maps are centered at the Pacific, as this region is only covered densely by the ship-log declination data. Clearly, uncertainties are lowest in the HistKalmag model, which is based on the full dataset. This model also shows lower intensity around the South Pole and a more constrained South Atlantic Anomaly. Another difference is the low intensity field patch over South East Asia. Location, shape and intensity of this patch are quite different among the three models. In the ArchKalmag14k.r model it is merged with the South Atlantic Anomaly. BIGMUDIh.1 also shows this patch, but it is merged with the South Atlantic Anomaly as well, separating later, around 1760 CE.

We show local model predictions, together with local data, in Figs. 4 and 5. Another location is provided with the supplementary material. In the seventeenth century, the Indian ocean was crossed by many ship voyages. The collected declination data lead to significant differences in the local predictions from the HistKalmag.no_D and
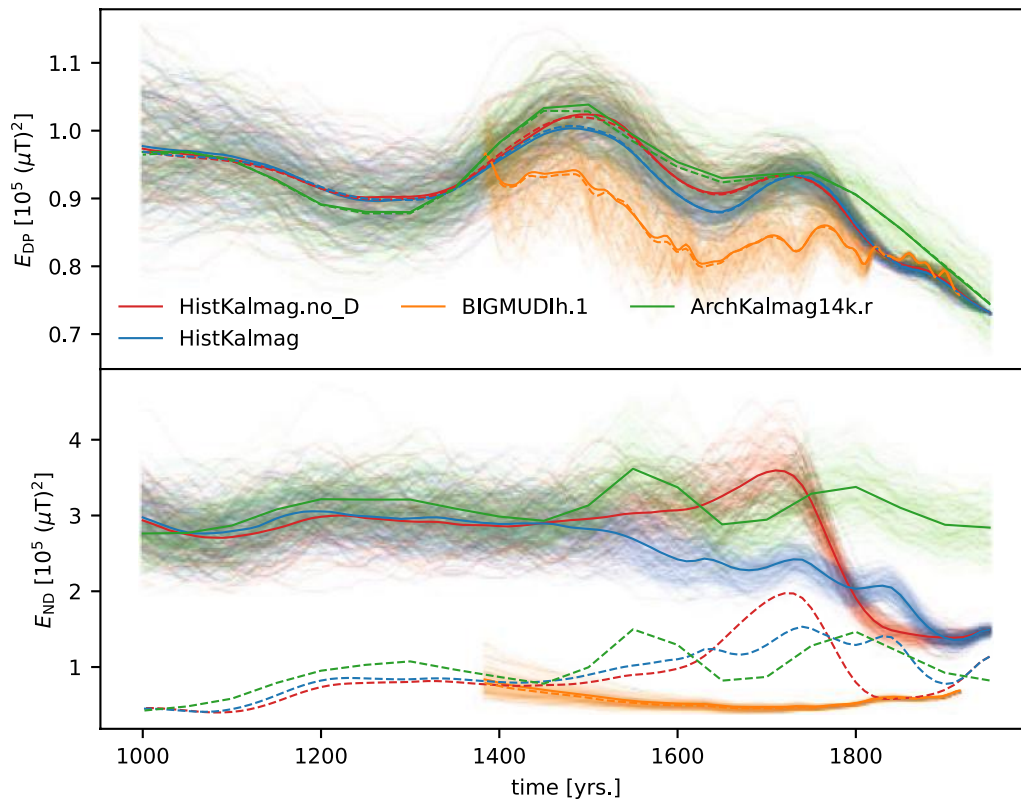
Fig. 2 Dipole (top) and non-dipole (bottom) energy at the core–mantle boundary. For ArchKalmag14k.r and the HistKalmag models, 100 samples from the posterior are drawn transparently in the background to illustrate the uncertainties. The thick lines give the ensemble mean, while the dashed lines represent the energy calculated from the mean model directly
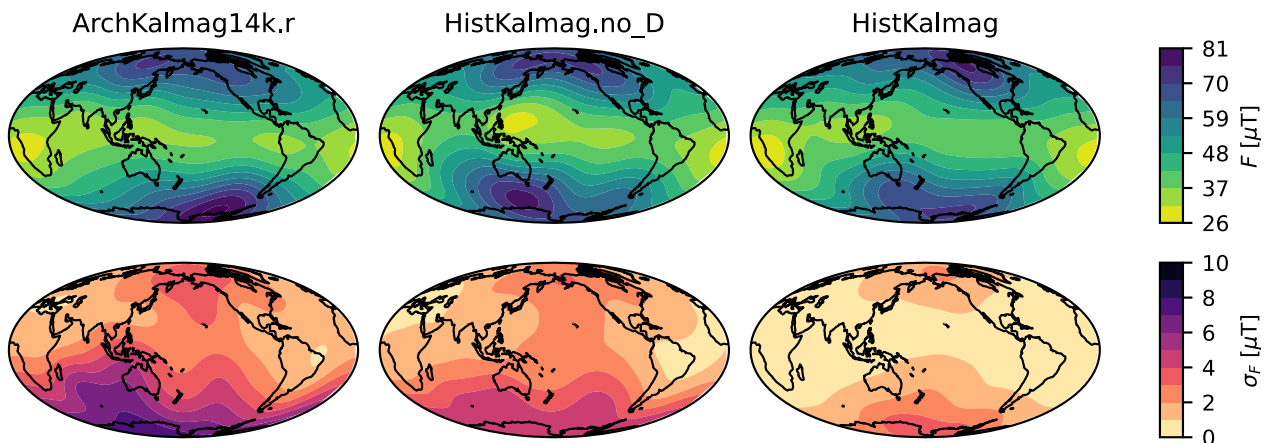
Fig. 3 Geomagnetic field intensity (top) and standard deviation (bottom) for the epoch 1700 CE. Depicted are the three models ArchKalmag14k, HistKalmag.no_D and HistKalmag. The maps are centered at the Pacific, as this region is covered densely only by the ship-log declination data

the HistKalmag model. Interestingly, this difference is not in the declination itself, but in the local predictions of the field intensity (Figure 4, top row). We believe this is again a consequence of global vs. local information. The HistKalmag.no_D model contains survey data from

India as well as inclination data from some ship voyages across the Indian ocean. These records contain intensity variations that are resolved locally by the model. Only the global coverage, introduced by the ship-log declination dataset, relates these features to global field structure,
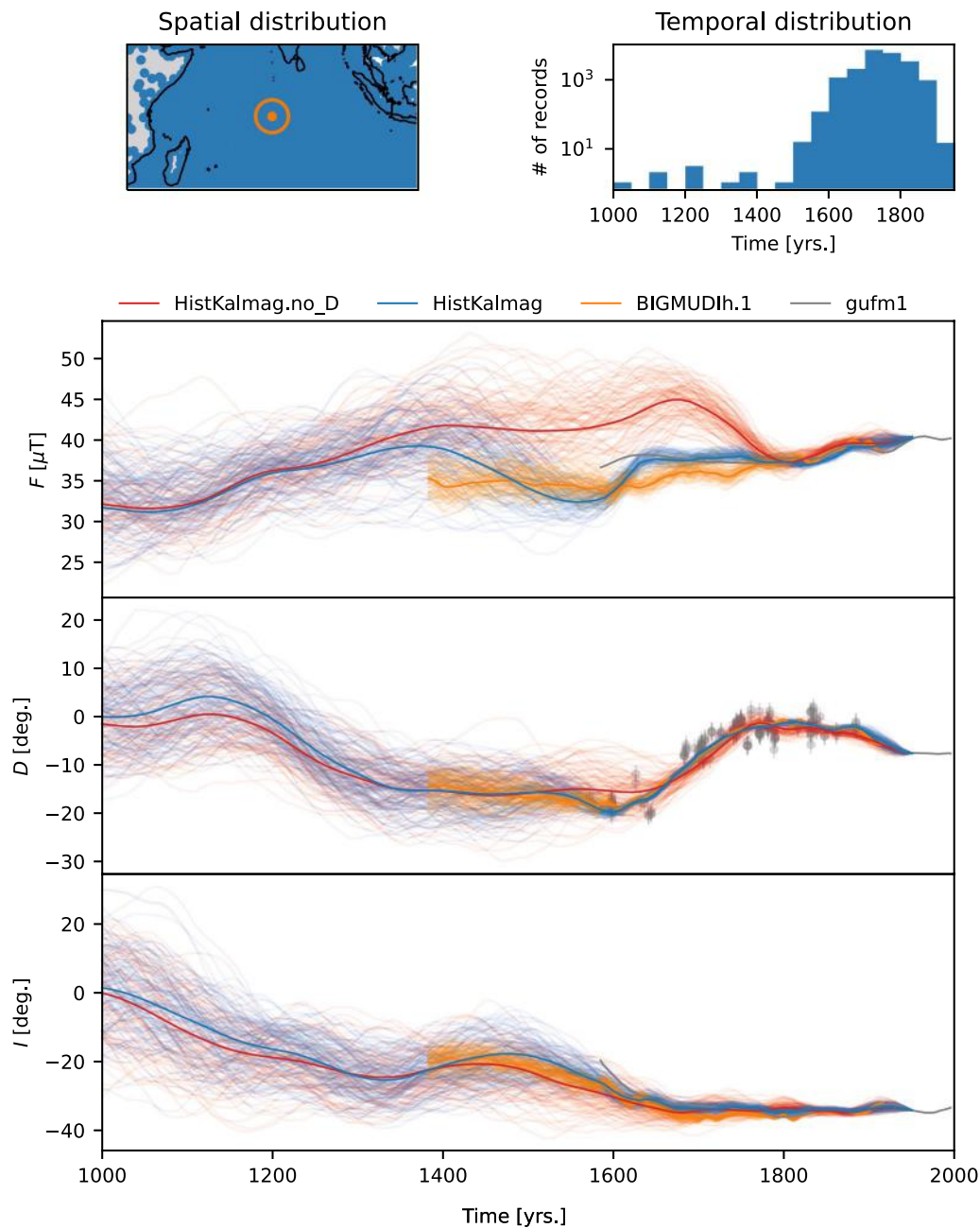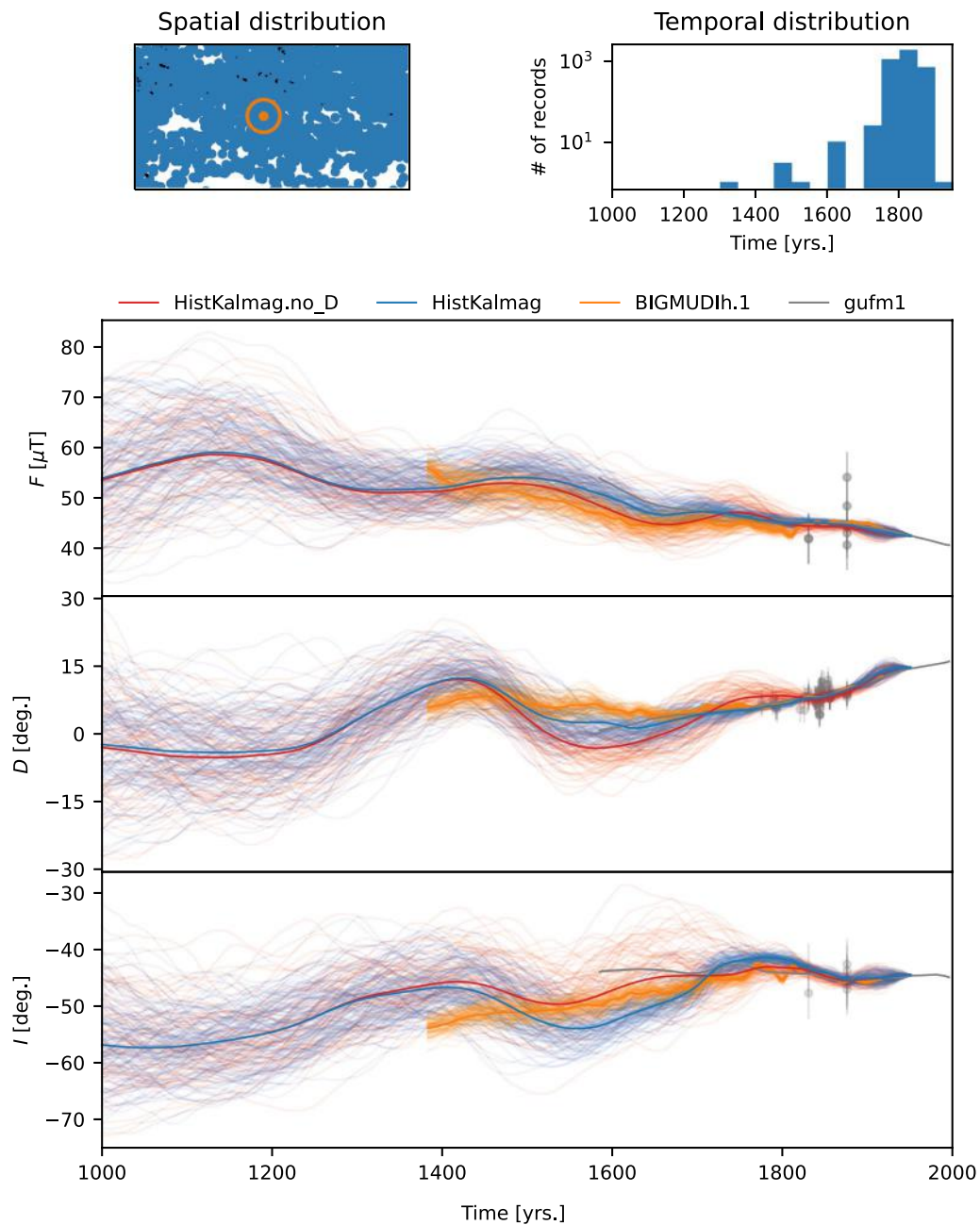
Fig. 4 Local predictions of three different models in the Indian Ocean (−6.5°, 73°), together with spatial and temporal distribution of the surrounding data. The upper right panel contains all records from the spatial distribution, while only data from a 500 km radius (depicted in orange in the top left panel) is shown together with the local predictions. The error bars reflect one standard deviation. Inclination and intensity are translated along the corresponding axial dipole (Merrill et al. 1996). 100 samples from the posterior ensemble are drawn as transparent lines in the background, to illustrate the model uncertainties

that also results in a locally different field intensity. Similar differences are visible in local predictions at the Azores (Additional file 1: Figure S6). However, the predictions there show some deviance for the declination as well. This may be due to the Azores being closer to Europe, which is densely covered by survey- and other

data from the eighteenth century, and by data from ship voyages across the Atlantic. The different global structure is also evident from Figs. 2, 3.

Even though no data is present in the direct surrounding, predictions at Rapa Iti, a small island in the

Fig. 5 Local predictions of three different models at Rapa Iti (−27.605556°, −144.344444°), together with spatial and temporal distribution of the surrounding data. The upper right panel contains all records from the spatial distribution, while only data from a 500 km radius (depicted in orange in the top left panel) are shown together with the local predictions. The error bars reflect one standard deviation. Inclination and intensity are translated along the corresponding axial dipole (Merrill et al. 1996). 100 samples from the posterior ensemble are drawn as transparent lines in the background, to illustrate the model uncertainties

Pacific, show a declination change around 1400 CE. This change is related to low intensity in the Pacific around this time (Additional file 1: Figure S7). The signal of low intensity is captured in intensity records

from the Pacific and North America and declination records from South America.
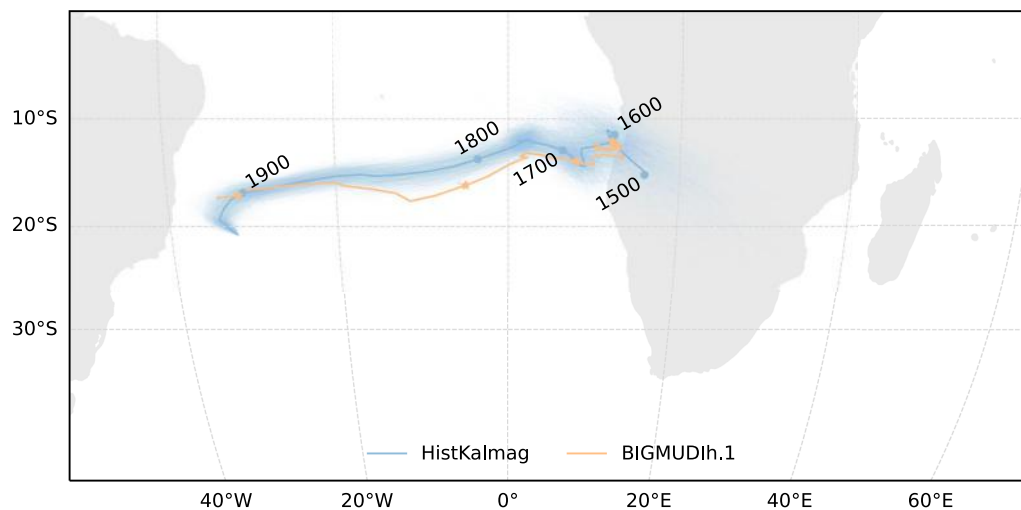
South Atlantic Anomaly

The South Atlantic Anomaly, a low-intensity field region in the South Atlantic region, has been investigated by several studies (e.g. Hartmann and Pacca 2009; Javier and Angelo 2016; Terra-Nova et al. 2017; Campuzano et al. 2019; Finlay et al. 2020). Recently, Hagay et al. (2021) proposed a novel definition of the South Atlantic Anomaly region and center of mass, taking global field changes into account. We consider the proposed definition and estimate area and center of mass of the South Atlantic Anomaly accordingly, extending the analysis of Hagay et al. (2021) further back in time. An animation of the evolution of the Earth's magnetic field intensity and radial component at the core–mantle boundary, together with uncertainties, is provided as supplementary material (Additional file 2).

The HistKalmag mean model shows a low-intensity field region over South East Asia in the beginning. This region splits, with one part quickly moving westward and the other decreasing and disappearing around 1100 CE.

The westward moving part stops its movement slightly north of South America and similarly splits, with one part decreasing and the other moving eastward. In the mean model, today's South Atlantic Anomaly appears as a merging of the decreasing part north of South America, that slightly moves eastward, and a low-intensity field patch emerging close to Madagascar around 1200 CE. However, individual realizations from the Histkalmag distribution show vastly different field configurations before ca. 1400 CE. The low intensity in the Pacific, depicted in Additional file 1: Figure S7, is the first feature that is consistent within the ensemble. Figure 6 shows the area of the low-intensity field region as defined by Hagay et al. (2021) (using their terminology, hereafter referred to as S1 region). The mentioned differing field configurations are also reflected in the S1 area, as evident from the spread in the sample curves depicted. After 1600 CE, the ensemble shows less variability around the mean, due to the increase in the number of data. This is the reason why we end the plot of the S1 center of mass (Fig. 7) at 1500 CE. Another reason is the aforementioned low-intensity region in the western Pacific. For some ensemble members intensity in this region is so low, that they
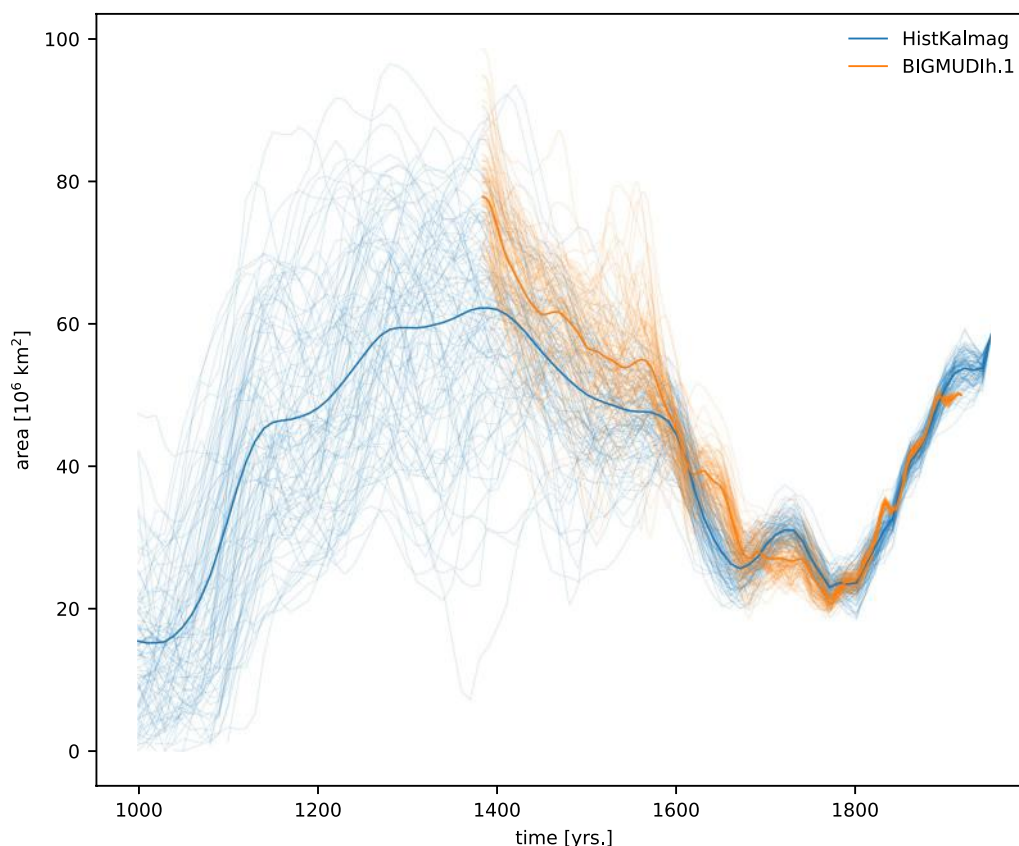
Fig. 6 Area of the S1 low-intensity field region over time, according to the definition by Hagay et al. (2021). The thick blue line corresponds to the HistKalmag mean model, the transparent lines in the background show the area of 1000 samples from the posterior distribution

Fig. 7 Location of the South Atlantic Anomaly center of mass, according to the definition by Hagay et al. (2021). The thick blue line corresponds to the HistKalmag mean model, the transparent lines in the background show the location of 1000 samples from the posterior distribution

show multiple low-intensity (S1) patches. Therefore, the center of mass of the whole region jumps abruptly and is not comparable to earlier epochs. To consistently track the center of mass, one would have to isolate the different patches, which is beyond the scope of this article. Evolution of both area and center of mass of the S1 region of the HistKalmag model are quite similar to BIGMUDIh.1, disagreeing most significantly before 1600 CE. The area decreases after 1500 CE, with two minima at 1680 CE and 1770 CE. The decrease is linked to the disappearance of a reverse flux patch at the core–mantle boundary at the southern tip of Africa. The rapid westward movement of the center of mass after 1700 CE is likely caused by the emergence of reverse flux patches in the western and central Pacific. Earlier, the center of mass is more stable as the associated flux patch at the core–mantle boundary moves only slightly. The described features are present in the mean model and most of the ensemble members, while fluctuations around the mean model are higher at the core mantle boundary than at the surface.

Conclusions

The HistKalmag model constitutes a bridge between the longer timescale ArchKalmag14k model and the satellite- and observatory era-based Kalmag model. The large database of direct, non-linear observations of the magnetic field from surveys and ship-logs provides global field information over the last five centuries. In order to assess what information can be extracted from declination records, an alternative model, HistKalmag.no_D, was constructed, where single declination records were disregarded. The model shows a higher non-dipole energy for the era covered by the declination dataset

than the HistKalmag model, which is built from the full dataset. The availability of more records helps notably to constrain global field properties like the dipole moment. A similar behavior is observed over longer timescales in the ArchKalmag14k model. However, more records also allow to resolve higher order degrees more accurately. Still, the general field structure is already captured well by the archeomagnetic database. This is likely due to the field sources lying deep inside the Earth and the resulting suppression of higher spherical harmonics. When looking at maps of the radial component at the core–mantle boundary (Fig. 8), one might get the impression that for recent times, when more data are available, the field shows more small-scale features. This is true for the mean field, however, samples from the posterior show a constant resolution (i.e., characteristic size of the posterior fluctuations) over the whole model period. The spread in the distribution is bigger for earlier times, leading to smoother (and thus larger spatial scale) patches in the mean. This highlights the importance of considering uncertainties when discussing model properties and features.

For the period covered by direct observations, we linked the South Atlantic Anomaly to reverse flux at the core–mantle boundary. For earlier times, uncertainties are too high to reliably locate features at the core–mantle boundary. Similar to Hagay et al. (2021), we find that the growth of low-intensity field patches is related to growth of reverse flux patches at the core–mantle boundary. The reverse flux patches at the core–mantle boundary are relatively static and instead of following their movement, the low-intensity field regions at the Earth's surface move from one patch to another (most notably, the South
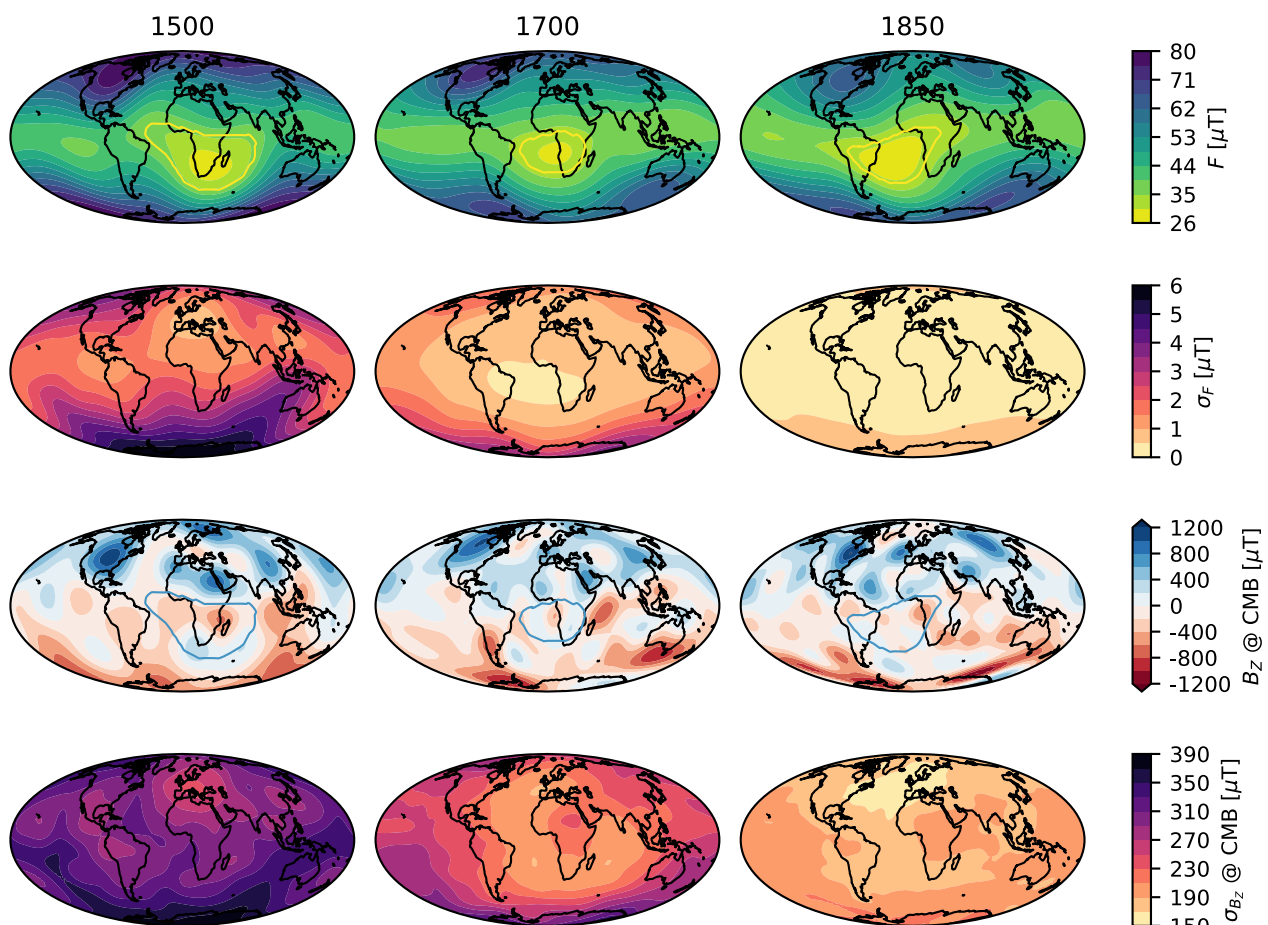
Fig. 8 The South Atlantic Anomaly at several epochs. The top row shows the field intensity at the Earth's surface, the second to bottom row the radial field component at the core–mantle boundary. The rows in between depict the standard deviations. The yellow/blue contour line indicates the S1 low field intensity region, according to Hagay et al. (2021)

Atlantic Anomaly is first located above a reverse flux patch at the southern tip of Africa and then "dragged" westward, by reverse flux appearing east of the coast of South America). By estimating the area of the South Atlantic Anomaly further back in time, we could extend the analysis of Hagay et al. (2021) and confirm their finding of a non-monotonous growth. More extremely, the South Atlantic Anomaly shrinks from 1500 CE to ca. 1600 CE and starts to grow rapidly after 1770 CE, with a milder growth and decrease in between.

During the development of the HistKalmag model many different parameter configurations of the modeling algorithm were tested. Parameters like the prior dipole strength or the model cutoff degree have an insignificant influence on the model. Further, the exclusion of outliers had only tiny influences on the model. We found that the most significant impact on the model was caused by considering different uncertainty levels for the data, in particular the abundant declination data. The modeling community would strongly benefit from consistently assessing the uncertainties in the historical dataset, and also in archeo- and paleomagnetic records.

Supplementary Information

The online version contains supplementary material available at https://doi.org/10.1186/s40623-023-01852-1.

Additional file 1: Figure S1. Composition of the dataset of indirect observations, together with spatial and temporal distribution. **Figure S2.** Composition of the full dataset, together with spatial and temporal distribution. **Figure S3.** Spatial power spectrum at 1500 CE for different models. The thin lines correspond to 100 ensemble members. **Figure S4.** Spatial power spectrum at 1700 CE for different models. The thin lines correspond to 100 ensemble members. **Figure S5.** Spatial power spectrum at 1800 CE for different models. The thin lines correspond to 100 ensemble members. **Figure S6.** Local predictions of three different models at the Azores , together with spatial and temporal distribution of the surrounding data. The upper right panel contains all records from the spatial distribution, while only data from a 500 km radiusis shown together with the local predictions. The errorbars reflect one standard deviation. Declination and intensity are translated along the corresponding axial dipole. 100

Schanner *et al. Earth, Planets and Space*   (2023) 75:96

Page 12 of 13

samples from the posterior ensemble are drawn as transparent lines in the background, to illustrate the model uncertainties. **Figure S7.** Evolution of a short lived low intensity region in the western Pacific around the year 1400 CE, calculated from the HistKalmag model. The top row shows the field intensity at the Earth's surface. The second row the field intensity standard deviation. The third row depicts the radial field component at the core mantle boundary and the bottom row the corresponding standard deviation. The yellow and blue contour line indicates the S1 low field intensity region, according to the definition by Amit et al..

Additional file 2. Animation of the HistKalmag model. The animation shows the temporal evolution of the geomagnetic field intensity at the Earth's surface and the radial component at the core mantle boundary (top row) together with the standard deviation (bottom row). Yellow and blue contour lines give the S1 Area according to Hagay et al. (2021).

Author contributions
MS, MK and CF designed this research. MK and CF performed data preprocessing and selection. MS performed theoretical work, analysis and software development. LB assisted in analyzing the impact of the hyperparameters on the model. MS assembled the manuscript, with contributions from all co-authors. MK and MH supervised the findings of this work.

Availability of data and materials
The dataset is a combination of the GEOMAGIA (Brown et al. 2015) and HISTMAG (Patrick et al. 2017) databases, which are freely available. A list of records identified as outliers is provided upon request. The modeling software is an extension of paleokalmag, wich is available via a git-repository https://sec23.git-pages.gfz-potsdam.de/korte/paleokalmag/. The HistKalmag model is also distributed via a dedicated website at https://ionocovar.agnld.uni-potsdam.de/Kalmag/Histo/ .

Declarations

Competing interests
The authors declare that they have no competing interests.

Author details
[1]Institute of applied mathematics, Potsdam University, 14467 Potsdam, Germany. [2]German Research Centre for Geosciences (GFZ) Potsdam, Potsdam, Germany. [3]GFZ Potsdam, Potsdam, Germany. [4]Potsdam University, Potsdam, Germany.

References
Alken P, Thébault E, Beggan CD, Amit H, Aubert J, Baerenzung J, Bondar TN, Brown WJ, Califf S, Chambodut A, Chulliat A, Cox GA, Finlay CC, Fournier A, Gillet N, Grayver A, Hammer MD, Holschneider M, Huder L, Hulot G, Jager T, Kloss C, Korte M, Kuang W, Kuvshinov A, Langlais B, Léger J-M, Lesur V, Livermore PW, Lowes FJ, Macmillan S, Magnes W, Mandea M, Marsal S, Matzka J, Metman MC, Minami T, Morschhauser A, Mound JE, Nair M, Nakano S, Olsen N, Pavón-Carrasco FJ, Petrov VG, Ropp G, Rother M, Sabaka TJ, Sanchez S, Saturnino D, Schnepf NR, Shen X, Stolle

C, Tangborn A, Tøffner-Clausen L, Toh H, Torta JM, Varner J, Vervelidou F, Vigneron P, Wardinski I, Wicht J, Woods A, Yang Y, Zeren Z, Zhou B (2021) International geomagnetic reference field: the thirteenth generation. Earth Planets Space 73(1):49. https://doi.org/10.1186/s40623-020-01288-x

Andreas N, Neil S (2021) Probabilistic approach to geomagnetic field modelling of data with age uncertainties and post-depositional magnetisations. Phys Earth Planet Inter. https://doi.org/10.1016/j.pepi.2021.106737

Arneitz P, Leonhardt R, Egli R, Fabian K (2021) Dipole and nondipole evolution of the historical geomagnetic field from instrumental, archeomagnetic, and volcanic data. J Geophys Res Solid Earth 126(10):e2021JB022565

Backus G, Parker R, Constable C (1996) Foundations of geomagnetism. Cambridge University Press, Cambridge

Baerenzung J, Holschneider M, Wicht J, Lesur V, Sanchez S (2020) The kalmag model as a candidate for IGRF-13. Earth Planets Space 72:163. https://doi.org/10.1186/s40623-020-01295-y

Baerenzung J, Holschneider M, Saynisch-Wagner J, Thomas M (2022) Kalmag: a high spatio temporal model of the geomagnetic field. Earth Planets Space. https://doi.org/10.1186/s40623-022-01692-5

Berrar D (2018) Bayes' theorem and naive bayes classifier. *Encyclopedia of Bioinformatics and Computational Biology: ABC of Bioinformatics; Elsevier Science Publisher: Amsterdam, The Netherlands*, pages 403–412

Bloxham J, Jackson A (1992) Time-dependent mapping of the magnetic field at the core-mantle boundary. J Geophys Res Solid Earth 97(B13):19537–19563. https://doi.org/10.1029/92JB01591

Bouligand C, Gillet N, Jault D, Schaeffer N, Fournier A, Aubert J (2016) Frequency spectrum of the geomagnetic field harmonic coefficients from dynamo simulations. Geophys J Int 207:1142–1157. https://doi.org/10.1093/gji/ggw326

Brown MC, Donadini F, Nilsson A, Panovska S, Frank U, Korhonen K, Schuberth M, Korte M, Constable CG (2015) Geomagia50.v3: 2. a new paleomagnetic database for lake and marine sediments. Earth Planets Space 67(1):70. https://doi.org/10.1186/s40623-015-0233-z

Campuzano SA, Gómez-Paccard M, Pavón-Carrasco FJ, Osete ML (2019) Emergence and evolution of the south atlantic anomaly revealed by the new paleomagnetic reconstruction shawq2k. Earth Planet Sci Lett 512:17–26. https://doi.org/10.1016/j.epsl.2019.01.050

Constable C, Korte M (2015) 5.09 - centennial- to millennial-scale geomagnetic field variations. In Gerald Schubert, editor, *Treatise on Geophysics (Second Edition)*, pages 309–341. Elsevier, Oxford, second edition. ISBN 978-0-444-53803-1. https://doi.org/10.1016/B978-0-444-53802-4.00103-2. https://www.sciencedirect.com/science/article/pii/B978044453802400103

Filipe T-N, Hagay A, Hartmann GA, Trindade Ricardo IF, Pinheiro Katia J (2017) Relating the south atlantic anomaly and geomagnetic flux patches. Phys Earth Planet Inter 266:39–53. https://doi.org/10.1016/j.pepi.2017.03.002

Finlay CC, Kloss C, Olsen N, Hammer MD, Tøffner-Clausen L, Grayver A, Kuvshinov A (2020) The CHAOS-7 geomagnetic field model and observed changes in the South Atlantic Anomaly. Earth Planets Space. https://doi.org/10.1186/s40623-020-01252-9

Gauthier H, Célinea E, Langlais B, Mioara M, Nils O (2002) Small-scale structure of the geodynamo inferred from Oersted and Magsat satellite data. Nature 416(6881):620–623. https://doi.org/10.1038/416620a

Gillet N (2019) Spatial And Temporal Changes Of The Geomagnetic Field: Insights From Forward And Inverse Core Field Models. In *Geomagnetism, aeronomy and space weather: a journey from the Earth's core to the sun*. https://hal.archives-ouvertes.fr/hal-02042703

Hagay A, Filipe T-N, Maxime L, Trindade Ricardo I (2021) Non-monotonic growth and motion of the South Atlantic Anomaly. Earth Planets Space. https://doi.org/10.1186/s40623-021-01356-w

Hartmann GA, Pacca IG (2009) Time evolution of the south atlantic magnetic anomaly. Anais da Acad Brasileira de Ciências 81:243–255. https://doi.org/10.1590/S0001-37652009000200010

Hellio G, Gillet N (2018) Time-correlation-based regression of the geomagnetic field from archeological and sediment records. Geophys J Int 214(3):1585–1607. https://doi.org/10.1093/gji/ggy214

Holschneider M, Lesur V, Mauerberger S, Baerenzung J (2016) Correlation-based modeling and separation of geomagnetic field components. J Geophys Res Solid Earth 121(5):3142–3160. https://doi.org/10.1002/2015JB012629

Javier P-CF, Angelo DS (2016) The south atlantic anomaly: the key for a possible geomagnetic reversal. Front Earth Sci 4:40. https://doi.org/10.3389/feart.2016.00040

Kalman RE (1960) A new approach to linear filtering and prediction problems. Trans ASME J Basic Eng 82(Series D):35–45

Korte M, Constable CG (2003) Continuous global geomagnetic field models for the past 3000 years. Phys Earth Planet Inter 140:73–89

Mauerberger S, Schanner M, Korte M, Holschneider M (2020) Correlation based snapshot models of the archeomagnetic field. Geophys J Int. https://doi.org/10.1093/gji/ggaa336

McHutchon A, Rasmussen C (2011) Gaussian process training with input noise. In: Shawe-Taylor J, Zemel RS, Bartlett PL, Pereira F, Weinberger KQ (eds) Advances in neural information processing systems 24. Curran Associates, Inc., pp 1341–1349

Merrill RT, McElhinny MW, McFadden PL (1996) The magnetic field of the earth: paleo-magnetism, the core, and the deep mantle. Academic Press, San Diego

Monika K, Catherine C, Fabio D, Richard H (2011) Reconstructing the holocene geomagnetic field. Earth Planet Sci Lett 312(3):497–505. https://doi.org/10.1016/j.epsl.2011.10.031

Nilsson A, Suttie N, Stoner JS, Muscheler R (2022) Recurrent ancient geomagnetic field anomalies shed light on future evolution of the south atlantic anomaly. Proc Natl Acad Sci 119(24):e220074911e2200749119. https://doi.org/10.1073/pnas.2200749119

Patrick A, Roman L, Elisabeth S, Balázs H, Franziska M, Peter K, Pavel H, Fridrich V, Gergely V, Christa H, Ramon E, Karl F, Niko K (2017) The HISTMAG database: combining historical, archaeomagnetic and volcanic data. Geophys J Int 210(3):1347–1359. https://doi.org/10.1093/gji/ggx245

Patrick A, Ramon E, Roman L, Karl F (2019) A bayesian iterative geomagnetic model with universal data input: self-consistent spherical harmonic evolution for the geomagnetic field over the last 4000 years. Phys Earth Planet Inter 290:57–75. https://doi.org/10.1016/j.pepi.2019.03.008

Roman L, Karl F (2007) Paleomagnetic reconstruction of the global geomagnetic field evolution during the matuyama/brunhes transition: Iterative bayesian inversion and independent verification. Earth Planet Sci Lett 253(1):172–195. https://doi.org/10.1016/j.epsl.2006.10.025

Schanner M, Mauerberger S, Korte M, Holschneider M (2021) Correlation based time evolution of the archeomagnetic field. J Geophys Res Solid Earth 126(7):e2020JB021548. https://doi.org/10.1029/2020JB021548

Schanner M, Korte M, Holschneider M (2022) Archkalmag14k: a kalman-filter based global geomagnetic model for the holocene. J Geophys Res Solid Earth 127(2):e2021JB023166. https://doi.org/10.1029/2021JB023166

Publisher's Note